



# Efficient prediction of tidal turbine fatigue loading using turbulent onset flow from Large Eddy Simulations

Hannah Mullings<sup>1</sup> · Lindsey Amos<sup>2</sup> · Calum Miller<sup>2</sup> · Pablo Ouro<sup>1</sup> · Tim Stallard<sup>1</sup>

Received: 9 May 2023 / Accepted: 3 April 2024  
© The Author(s) 2024

## Abstract

To maximise the availability of power extraction from a tidal stream site, tidal turbines need to be able to operate reliably when located within arrays. This requires a thorough understanding of the operating conditions, which include turbulence, velocity shear due to bed proximity and roughness, ocean waves and due to upstream turbine wakes, over the range of flow speeds that contribute to the loading experienced by the devices. High-fidelity models such as Large Eddy Simulation (LES) can be used to represent these complex flow conditions and turbine device models can be embedded to predict loading. However, to inform micro-siting of multiple turbines with an array, the computational cost of performing multiple simulations of this type is impractical. Unsteady onset conditions can be generated from the LES to be used in an offline coupling fashion as input to lower-fidelity load prediction models to enable computationally efficient array design. In this study, an in-house Blade Element Momentum (BEM) method is assessed for prediction of the unsteady loads on the turbines of a floating tidal device with unsteady inflow developed with the in-house LES solver DOFAS. Load predictions are compared to those obtained using the same unsteady inflow to the commercial tool Tidal Bladed and from an Actuator Line Model (ALM) embedded in the LES solver. Estimates of fatigue loads differ by up to 3% for mean thrust and 11% for blade root bending moment for a turbine subject to a turbulent channel flow. When subjected to more complex flows typical of a turbine wake, the predictions of rotor thrust fatigue differ by up to 10%, with loads reduced by the inclusion of a pitch controller.

**Keywords** Tidal turbine · Unsteady loading · Blade element momentum method · Large Eddy Simulation · Actuator line model

## 1 Introduction

In 2022 and 2023, 94MW of tidal stream energy projects were awarded under the UK Government's contracts for difference scheme. This is the main mechanism for the UK Government to support low carbon power generation, to give a reasonable strike price for industry to commit to sources of renewable energy. This is a step forward for the sector, but still requires appropriate research and development, particularly to further the understanding of methodologies suited to design of the arrays of tidal turbines needed to fulfil the allocated megawatts of power generation. The tidal stream resource

within the UK is significant in terms of flow speeds and the available kinetic energy flux. However, due to the nature of the environment in which turbines operate, there are several factors which result in a complex onset flow to each turbine. Existing design standards, IEC-62600 or DNV-GL (2015), list these factors as a mixture of velocity shear, turbulence and waves. These standards are mostly adaptations of their wind energy counterparts and for tidal stream, the extent to which these flow characteristics influence unsteady loading varies with site, deployment position within the site as well as depth and the device type. There are a variety of types of tidal energy converters from kites to vertical axis turbines to more recognisable horizontal axis turbines. All of these device types have been trialled at full scale, with the development of arrays ongoing in the UK, France and Canada, typically involving the deployment of horizontal axis turbines.

The extent to which different environmental factors influence horizontal axis turbine loading is influenced by whether

✉ Hannah Mullings  
hannah.mullings@manchester.ac.uk

<sup>1</sup> School of Engineering, The University of Manchester, Oxford Road, Manchester M13 9PL, UK

<sup>2</sup> Innovation Centre, Orbital Marine Power, Hatston Pier Road, Kirkwall, Orkney KW15 1ZL, UK

they are bed-mounted or floating, as shown in Mullings and Stallard (2021), Stansby and Ouro (2022) and Mullings et al. (2023). When considering vertically sheared onset flow conditions, floating turbines located near the surface are in a good position for maintenance work on the device and will experience higher onset velocities. However, this position means they are more exposed to wave loading when compared to bed-mounted devices, Díaz-Dorado et al. (2021). In contrast bed-mounted devices are subjected to bed generated turbulence and a more severe shear profile, as shown in Parkinson and Collier (2016), Ahmed et al. (2017), Harrold and Ouro (2019), Ouro and Stoesser (2018) and Mercier et al. (2020).

In addition to considering the environmental conditions as an influence on the onset flow field, as the sector develops more research is required to determine how turbines operate in large arrays. A turbine located within an array will be subject to the effects of blockage generated between adjacent turbines, and to the wakes from upstream devices. Some of these effects have been investigated both experimentally and computationally in Masters et al. (2013), Stallard et al. (2013), Stansby and Stallard (2016), Ouro and Nishino (2021), Ouro et al. (2023) and McNaughton et al. (2022).

Methods for determining the loads and performance from these combinations of unsteady onset flow conditions vary from experimental to computational simulations. This study focuses on computational methods of various fidelity levels to simulate a turbulent onset flow field and the resultant unsteady loading experienced by a horizontal axis tidal turbine. Steady state performance of a turbine can be assessed using Blade Element Momentum theory (BEM) where the geometry of the turbine, aerodynamic properties of the blades and the onset flow speed are required as input to the model. When assessing the unsteady and time varying loading on a turbine it is important to include velocity fluctuations as inflow to the model, to represent measured turbulent conditions. Previous studies have utilised spectral models, sometimes referred to as the Sandia method, due to their application to creating three-dimensional wind flow fields, Veers (1988). In this approach power spectral densities (PSD) across a grid of discretised points are combined with a coherence function to create the flow field. The von Kármán spectrum is commonly used to provide a suitable PSD of the stream-wise velocity for the application of tidal stream, as seen in Milne et al. (2013), Parkinson and Collier (2016), Mullings et al. (2019), Togneri et al. (2020). Comparisons in Mullings and Stallard (2022) and Togneri et al. (2017) have been made using this method and with a flow field generated using a synthetic eddy method, developed by Jarrin et al. (2006). Both methods can be used at low computational cost to provide a suitable inflow to a BEM type model. How-

ever, such flow fields are typically propagated using Taylor's frozen turbulence hypothesis. As such the flow field does not allow for any interaction between the turbine and the onset flow. Whilst this is still a suitable method to create and use an unsteady onset flow field, further parameters are required to consider multiple devices in rows which will cause a velocity deficit in the wake of an upstream device.

Semi-empirical wake models have been used in previous work, Mullings et al. (2019a), to allow for the influence of wakes to be considered with these flow field models. An alternative, albeit more computationally expensive approach that provides an established wake within the flow field, is to use computational fluid dynamics (CFD) to generate an unsteady flow simulation. One or more tidal devices can also be included in such simulations. With the inclusion of turbulence, Reynolds averaged Navier–Stokes (RANS) equations can be used to model the flow within the domain, but an improvement in the resolution of fluctuating loads is obtained when Large Eddy Simulation (LES) is used, Afgan et al. (2013). In these numerical frameworks, the tidal device can be modelled by an Actuator Line Model (ALM), within a RANS model as seen in Apsley and Stansby (2020) and with LES as in the case of the DOFAS in-house code in Ouro and Nishino (2021). This method allows tip vortices and the far wake to be captured enabling the turbine to turbine interactions to be well resolved within the flow field.

This study investigates the variation in unsteady loading predictions from two different turbine load models: an LES-ALM model and BEM theory. The axial loading on the blades and rotor are determined to provide thrust forces and root bending moments to calculate fatigue loads. These forces will be calculated for a device experiencing representative conditions at an upstream location and for downstream devices operating in a wake. Inflow to the unsteady BEM is defined by output planes from the LES, to determine whether this combination of models can predict loading at a lower computational cost than running computationally-expensive full LES-ALM for multiple downstream turbine positions.

The paper will follow this format; Sect. 2 will describe the set up of the numerical models and include the geometry of the turbine, the site conditions represented and the method for quantifying the fatigue; Sect. 3 will focus on the loading experienced on a single device, both upstream and downstream, for each device scale model; and Sect. 3.3 will investigate the loading experienced on a downstream device at various positions in the wake; and Sect. 3.4 assesses the potential impact of a basic pitch control on the loading. A discussion is given in Sect. 4, before the conclusions are drawn in Sect. 5.

## 2 Set up of numerical models

### 2.1 Turbine specification

The tidal device modelled here consists of two turbine rotors each with two blades, following the configuration of a full scale floating device as documented by Orbital Marine Power (2022), as their 20 m diameter O2 device, sketched in Fig. 1, operating at a single tip-speed-ratio (TSR) of 5.5. Modelling turbines computationally can be performed in different ways as introduced in Sect. 1. In this study, two types of load prediction models are employed, using blade element momentum theory and an actuator line method, and their results compared.

### 2.2 The in-house BEM model

Firstly, blade element momentum theory has been adopted for both steady and unsteady conditions. This model has been applied using two different implementations, one is the commercial code Tidal Bladed widely used in the Tidal Stream Energy sector, for example in Parkinson and Collier (2016), and the other is an in-house unsteady blade element code which has previously been validated against experimental work in Mullings et al. (2019) and Mullings and Stallard (2022).

The BEM presented in Mullings and Stallard (2022) and employed here extracts the onset flow at ‘N’ positions along a blade length, which rotate with time, depending on the chosen operating point. The onset flow is used to determine the relative onset flow ( $U_{rel}$ ) and inflow angle ( $\phi$ ) to the blade at each radial position ( $r$ ) along the blade, as shown by Eqs. 1–2.

$$\delta U_{rel}(t) = \sqrt{(U_x(1 - a))^2 + ((\omega r - U_\Theta)(1 + a'))^2} \quad (1)$$

$$\delta\phi(t) = \sin^{-1} \frac{U_x(t)}{U_{rel}(t)} \quad (2)$$

where  $U_{rel}$  is the relative velocity to the blade which incorporates the longitudinal velocity,  $U_x$  is the stream-wise onset

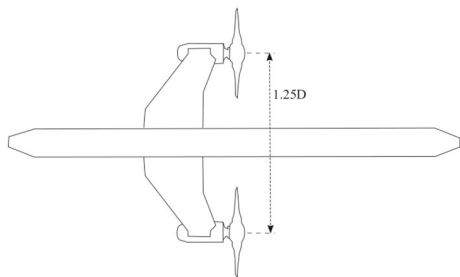


**Fig. 1** Top down view of the O2 Device, highlighting spacing between the turbine rotors, where  $D$  is the rotor diameter, with a vertical spacing of approximately  $0.15D$  to the free surface

velocity which includes in axial induction ( $a$ ) and the components in the tangential direction,  $U_\Theta$  with the angular velocity  $\omega$  and each radius  $r$ , with tangential induction,  $a'$ . The lift and drag force on each blade segment vary according to Eqs. 3–4.

$$\delta L(t) = \frac{1}{2} B \rho c (U_{rel})^2 C_L \delta r \quad (3)$$

$$\delta D(t) = \frac{1}{2} B \rho c (U_{rel})^2 C_D \delta r \quad (4)$$

where  $c$  is the chord length,  $\delta r$  is the radial width of the blade segment,  $B$  is the number of blades, here  $B = 1$  as the forces are calculated per blade,  $\rho$  is the fluid density,  $C_L$  and  $C_D$  correspond to the lift and drag coefficients respectively. Noting here that the angle of attack is determined using the inflow angle, the twist and any pitch of the blade. As well as the angle of attack the lift and drag polars are provided, for a Reynolds number range of  $1 \times 10^6$  to  $15 \times 10^6$ , where the local Re number is determined per blade segment. Using the calculated lift and drag forces for each blade the axial ( $F_a$ ) and tangential ( $F_t$ ) forces along each blade are calculated using Eqs. 5–6.

$$\delta F_a(t) = \delta L(t) \cos(\phi(t)) + \delta D(t) \sin(\phi(t)) \quad (5)$$

$$\delta F_t(t) = \delta L(t) \sin(\phi(t)) - \delta D(t) \cos(\phi(t)) \quad (6)$$

The axial force ( $F_a$ ) on each segment of the blade leads to the calculation of root bending moment as well as rotor thrust. These results can be used to establish the respective load spectra and hence determine the load cycles enabling the fatigue loads to be predicted by the summation of Eqs. 5 and 6 across all blades defining the rotor.

This version of the in-house BEM is used to compare with an actuator line method, detailed in the next section, therefore the sub-models used include tip and hub losses through Prandtl’s tip loss and an induction model is applied using the Glauert high-axial-induction correction, but did not include dynamic stall or inflow. The Tidal Bladed simulations which were run included the same sub-models and additional sub-models, such as, dynamic inflow through using the method of Pitt and Peters (1980) with a Øye dynamic wake model. Hydrodynamic added mass is also included, but no wake skew or dynamic stall is included in either model. The loading using the in-house BEM, with a simple pitch controller, has also been included. This controller is dependant on the flow speed and the function used has been calibrated to provide resultant time-varying loads which compare to a full-scale dynamic controller.

### 2.3 DOFAS: in-house LES code

The Digital Offshore Farms Simulator (DOFAS) in-house code, Ouro et al. (2019), adopts the spatially-filtered Navier–Stokes equations with the large-eddy simulation (LES) turbulence closure, which resolves the turbulent scales larger than the grid size. LES captures the energetic large-scale vortices present in open-channel and tidal flows and those turbulent structures introduced by tidal turbines. A second-order finite difference scheme is used to approximate the fluxes, solved in a rectangular Cartesian grid with staggered storage of velocities. A fractional-step method is adopted to advance the simulation in time using a fully-explicit scheme with a predictor-corrector three-step Runge–Kutta method. The Poisson pressure equation is solved with an algebraic multi-grid method. The WALE sub-grid scale model is adopted.

DOFAS adopts an Actuator Line Method (ALM) to resolve the turbine blades, with anisotropic interpolation functions that provide an improved force communication between fluid and structural meshes, Ouro and Nishino (2021), as the spreading kernels are different in the three spatial directions and vary with the chord length at every Lagrangian marker. The corresponding interpolation function  $g_L$  reads:

$$g_L(x, y, z) = \frac{1}{\varepsilon_x \varepsilon_y \varepsilon_z \pi^{3/2}} \exp \left( -\frac{(x - x_L)^2}{\varepsilon_x^2} - \frac{(y - y_L)^2}{\varepsilon_y^2} - \frac{(z - z_L)^2}{\varepsilon_z^2} \right) \quad (7)$$

where  $\varepsilon_x = 0.2c$  and  $\varepsilon_y = \varepsilon_z = 0.4c$ , with  $c$  indicating the chord length at the ALM point following (Martínez et al. 2018). The use of ALM enables the use of relatively coarse grid resolutions without the need for explicitly resolving the rotor geometry, which alleviates the inherent computational cost of performing LES, Stansby and Ouro (2022). In the present simulations, a total of 53 grid points are distributed across the turbine's rotor diameter, and a Prandtl correction is adopted to account for tip losses, as per the implementation by Shen et al. (2005). Ouro et al. (2019) validated the accuracy of this LES-ALM method in DOFAS in terms of hydrodynamic coefficients and turbulent flow statistics in the wake of small-scale tidal turbine arrays, and has been used in the application of waves with turbulent flow structures, Ouro et al. (2024).

The numerical domain is 1,152 m long, 480 m wide and 42 m deep, presented in Fig. 2, adopting a uniform grid resolution in the three spatial directions equal to 0.0375 m, which provides a total number of mesh elements of  $3,072 \times 1,280 \times 112$  per direction respectively, i.e. a total of 440.4 million cells. Regarding the time integration, a fixed time step is considered with a value of 0.0475 s. A total of 70,000 time steps are computed to simulate more than 3,300 s

of physical time using 200 CPUs on the local CSF cluster at The University of Manchester (UK).

At the inlet, a 1/7th power-law vertical shear profile with a mean velocity of 2.5 m/s at hub height is adopted with an imposed turbulence intensity of 12% as typically found at tidal sites, which was generated using an anisotropic Synthetic Eddy Method (SEM) with length-scales of 50 m, 20 m and 15 m, in  $x$ -,  $y$ - and  $z$ -direction respectively. These are set to have an averaged streamwise turbulence length similar to the water depth and keeping an anisotropy ratio of 1:0.4:0.3 similar to those found at some tidal sites, Garcia-Novo and Kyozuka (2017, 2019). At the outlet a Neumann boundary condition was used, with a slip condition applied at the lateral boundaries. A wall-function for hydro-dynamically smooth bed was adopted at the bottom boundary, as the large Reynolds number of the present simulations leads the first grid cell from the bottom wall to be located outside of the viscous sub-layer. At the free-surface top boundary, a shear-free rigid lid approach is used, in which vertical velocities and vertical gradients of horizontal velocity components are zero.

### 2.4 Quantifying fatigue loads

The loading experienced by both turbines of the device varies due to the unsteady conditions in the onset flow. Time varying loading is calculated using the previously mentioned BEM theory and the LES-ALM. This time varying loading is analysed to determine the number of load cycles the turbine components experience over the simulated period. In this case one quasi-steady interval is used, of approximately 300 s.

The load cycles are calculated using the results for each modelling method using Rainflow Cycle Counting, as described in Downing and Socie (1982). This method allows cycles with varying amplitude to be counted, rather than cycles of a constant magnitude. This method has been applied to determine the load cycles and therefore fatigue loads on offshore components by Parkinson and Collier (2016) and Weller et al. (2015). These load cycles are then used as a basis to determine the cyclic load fluctuations and equivalent loading the turbine will experience over a specified period of time when operating in these conditions. This equivalent loading is called the Damage Equivalent Load (DEL) and is derived using linear damage hypothesis to provide a single magnitude load repeating at a single frequency. Equation 8 defines the DEL, where  $n_i$  is the number of cycles at each binned load magnitude,  $m$  is the material gradient,  $f$  is the repetition frequency,  $T$  is the time period,  $L_i$  is the load bin, and  $L_m$  is the damage equivalent load for specific material gradient.

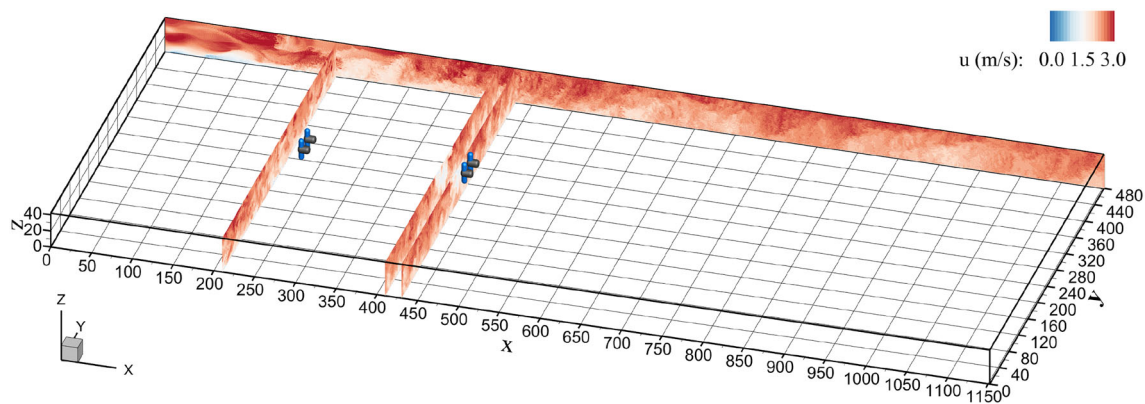


**Fig. 2** Representation of the computational domain used in the LES, including the two tidal turbine devices. Cross-sections included indicate locations where inflow data have been extracted to do the offline coupling with BEM models, showing values of instantaneous streamwise velocity ( $u$ )

$$L_m = \left( \frac{\sum_i n_i L_i^m}{fT} \right)^{1/m} \quad (8)$$

This method is used in the design standards (DNV-GL 2015) to calculate fatigue loading.

## 2.5 Onset flow conditions

The onset flow conditions to the turbine need to be defined. In this study the turbulent flow field is created using the LES from the DOFAS code. This enables instantaneous turbulent velocity data acquisition at cross-sectional planes of interest, at specific downstream locations within the computational domain, depicted in Fig. 2. Three onset flow datasets from two simulation setups have been considered, namely modelling only the upstream turbine and extracting data at  $1D$  upstream of it and at a nominal downstream distance of  $10D$ , a location at which a second turbine is then modelled in another simulation set-up, with planes extracted at  $1D$  upstream, i.e.  $9D$  downstream of the first device. This approach is equivalent, as an inflow, to creating onset flow fields from a statistical or synthetic turbulence model such as the von Kármán or Kaimal models, superposed with a mean shear flow. The duration of these datasets is 600 s (10 min) as time-window specified in IEC-62600 standards for load assessment. Hence, in the following, time averaging operation is referred to as the mean values computed over this sampling period of 600 s, generated during the physical time between 2,700 and 3,300 s of the LES.

The site conditions for the floating device modelled here are chosen as generic conditions. At the turbine location, the simulations feature a mean stream-wise velocity of 2.5 m/s, a resultant turbulence intensity across the rotor of 10% and length-scales in the range of 15–20 m.

### 2.5.1 Upstream device

The single device operating in the upstream experiences similar turbulence characteristics to those pre-defined at the inlet of the LES in the DOFAS code, as the flow develops from the inlet until encountering the turbine. The onset planes are then considered one diameter upstream of the modelled devices. The spatial distribution of the time averaged stream-wise velocity at  $-1D$  upstream of the device is shown in Fig. 3a in which the position of the two rotors from the device are also shown. The time averaged velocity shows the vertical shear, where higher velocities are found nearer to the surface, and the presence of the two ALM rotors causes a small decrease in the onset flow. The variation of stream-wise turbulence intensity is shown in Fig. 3b, along with the turbine positions within the domain.

For both turbine positions the vertical profiles of velocity and turbulence intensity are extracted as time averaged, as shown in Fig. 4. These profiles are examined at the hub location of the rotors, and for the velocity profile, compared to the pre-defined depth variation of a  $1/7$ th power law profile. It can be seen that the upstream plane at  $-1D$  where turbines are located at  $0D$ , allows the turbine to experience the shear profile that is used as input. The turbulence intensity however, does vary across the rotor area, from an input of 10% in the set up of the domain. Figure 4b shows that rotor one will experience higher intensity for the bottom half of the rotor than rotor two, which will experience higher intensity towards the top of the rotor. Although this is true at this horizontal position in the domain, Fig. 3b shows a variation across the domain with the rotors experiencing on average a  $\pm 2\%$  around the pre-defined 10%. This is the case because for a time window of 600 s or similar, TI values are not fully converged so variation is expected, the objective here is to generate time varying onset flow planes, not necessarily fully converged values.

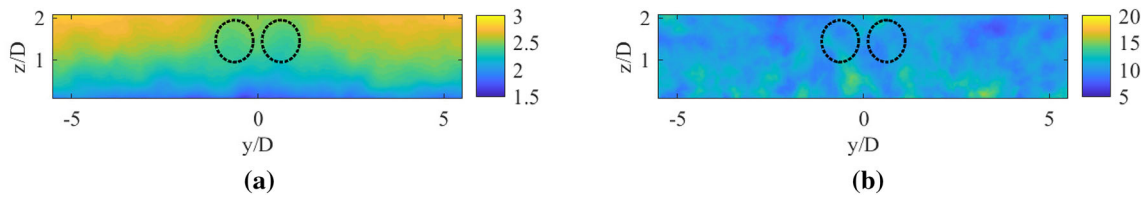


**Fig. 3** Variations of onset flow characteristics across the upstream plane, with rotor locations shown by dashed lines, **(a)** Time averaged stream-wise velocity, (m/s), **(b)** Stream-wise turbulence intensity, (%)

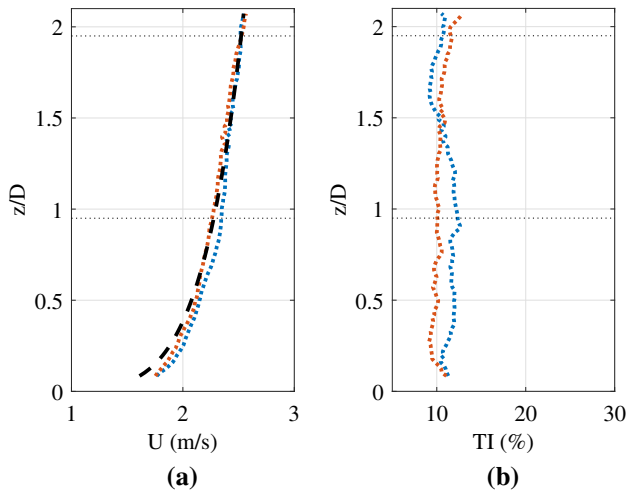


**Fig. 4** **a** Vertical variation of stream-wise velocity at the centre of each rotor compared to a 1/7th power law profile (dashed line), **b** vertical variation of turbulence intensity at the centre of each rotor. Rotor one position (blue), rotor two position (orange) (colour figure online)

## 2.5.2 Multiple devices

The previous onset flow characteristics across the domain corresponded to the upstream plane only at  $x = -1D$ . This plane can be used as an inflow to a turbine operating on the first row of an array, as will be shown in this work, and can also be used as inflow with the inclusion of other wake models, such as a Gaussian wake. In arrays, the downstream turbines will experience the wake generated from upstream devices which are explicitly modelled in DOFAS. The characteristics of the inflow to that device will be examined in this section, with two cases used. The first case relies upon LES with one device only, at  $x = 0D$ . A downstream plane is extracted, at a nominal distance of  $10D$  downstream to provide an unsteady velocity field that will be used as a basis to determine the difference to the ambient conditions. The second case considers both the upstream device and second device, located at the nominal distance of  $10D$  downstream, and from which the plane at  $9D$  is extracted (i.e.  $1D$  upstream of the downstream turbine). This latter case provides an insight into how the induction changes with the inclusion of a downstream turbine within the domain.

The extraction of the onset flow plane for these two cases allows for the comparison of onset flow characteristics and the loading generated on the second device computed with the ALM, to be compared with the loading predicted from the BEM methods. Figure 5 shows the transverse variation of the stream-wise velocity and the turbulence intensity averaged during the 600 s duration of the onset data. In comparison to Fig. 3a, the stream-wise velocity variation in Fig. 5a shows a reduction in velocity which is aligned to the location of the two upstream rotors from the tidal device. The variation of turbulence intensity between the upstream and downstream positions has also been affected by the wake of the upstream device, with increases in intensity observed over the rotor area, with rotor one more affected than rotor two, over the 600 s sample time.

As with the upstream plane, the vertical variation of the time averaged stream-wise velocity and turbulence intensity is extracted at the hub locations of both secondary rotors, i.e. at  $10D$  downstream, as shown in Fig. 6. The depth profile of velocity for the upstream location has a reduced value of velocity across both rotors, caused by the wake of the upstream device. This reduction in velocity also provides a different trend across the rotor, with the bottom of the rotation experiencing a slightly higher velocity than the top of the rotor, which does not correspond to the 1/7th profile. As observed with the variation across the horizontal plane, an increase in turbulence intensity is seen across the depth at the hub positions, with rotor one experiencing a turbulence intensity of 18%, at the same depth that rotor two is experiencing 11%. Across the rotor depth, rotor two experiences a turbulence intensity around the pre-defined 10% at some depths, whereas across rotor one the vertical variation shows that the intensity is above this. The difference in characteristics between the two rotors corresponds to a slightly asymmetric wake, due to the direction of rotation of each rotor, and the fact that the wake for these devices are a combination of two individual wakes merging with progression downstream over a relatively short averaging time of 600 s.

The onset flow characteristics for the second downstream case with the plane extracted at nine diameters downstream of an upstream device are shown in Fig. 7. The stream-wise velocity variation is shown to have a greater deficit than for the extracted plane at ten diameters downstream. The

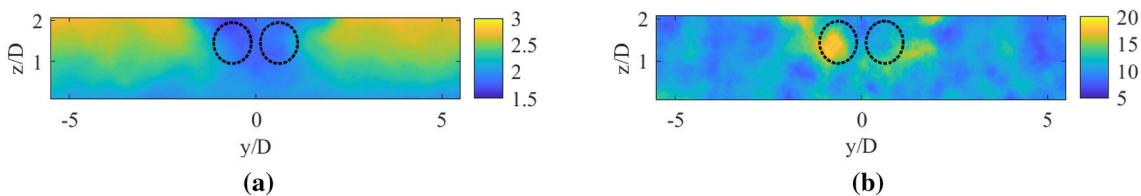


**Fig. 5** Onset flow characteristics across the plane at a distance of ten diameters behind an upstream rotor, with rotor locations shown by dashed lines, **a** Time averaged stream-wise velocity, (m/s), **b** stream-wise turbulence intensity, (%)

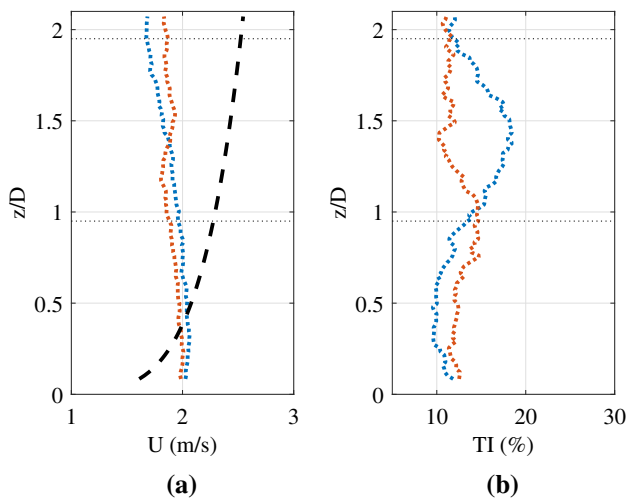


**Fig. 6** For a plane at ten diameters downstream of an upstream device, **a** vertical variation of stream-wise velocity at the centre of each rotor, **b** vertical variation of turbulence intensity at the centre of each rotor. Rotor one (blue) and rotor two (orange) (colour figure online)

maximum deficit has been shown, Stallard et al. (2013), to decrease as the turbine moves further away in the longitudinal direction, so this can account for the difference. However, the addition of the second ALM device with the two rotors located only one diameter downstream will show a small amount of induction, as seen in the upstream case. There are also differences in the turbulence intensity between the downstream planes, with a wider influence of the wake across the domain, due to the shorter distance for the nine diameter case. There is also a slight decrease in the ambient turbulence on either side of the wake, which may affect the loading on devices placed in offset positions to the wake.

The vertical profiles of stream-wise velocity and turbulence intensity at the horizontal rotor hub positions are given in Fig. 8. At this downstream position both rotors experience a very similar magnitude and variation of velocity, as the deficit due to the wake dominates across the rotor area. As with the other downstream plane, the shear profile defined at the inlet visible in the upstream plane is not observed in the wake when the two rotors are directly aligned with the upstream device. However, examining the plane width it is clear that if vertical profiles were extracted in offset transverse positions across the domain, then a sheared profile

would be present. The vertical profiles of turbulence intensity show much closer agreement between the two rotors across the rotor depths, than observed for the plane at ten diameters downstream. Across the rotor depths this intensity is greater than the original definition at the inlet of the domain and greater than experienced by the upstream device. Use of these different planes allows for the variation of conditions due to the wake of the rotors in this model to be accounted for.

The combination of the variation in turbulence in the wake with the velocity in the flow fields will be used as input into both the in-house BEM and Tidal Bladed, to draw comparisons with the loading calculated using the LES-ALM in the next Section. In addition, the impact of the flow fields can be investigated for a device located at different transverse positions. Initially, the conditions the turbine will experience are shown in Fig. 9 as disk averages.

The disk averaged conditions have been calculated for both downstream planes, for a device located in the original aligned location and for four other devices located at intervals of one diameter offset positions ( $y = -1D, -2D, -3D, -4D$ ). Values of the disk averaged velocities at both downstream locations, for the devices furthest left ( $y = -3D, -4D$ ) the values for both rotors, are within 1% and comparable to the upstream velocity. Rotors are positioned closer to the wake of the upstream device, experience shear, as shown in the downstream planes, Fig. 9. From the sheared flow, and in towards the greatest velocity deficit, causes a gradual reduction in velocity, with the flow fields at nine diameters downstream causing the lowest disk averaged velocities, consistent with the observations from the time averaged planes.

The disk averaged turbulence intensities are calculated in the same manner as the velocities. For each calculation the intensity is determined using the mean upstream onset flow rather than the local mean to facilitate comparison to the upstream intensity variation. These intensities are seen to vary with transverse rotor location consistent with the planes from both downstream flow fields. The nine diameter downstream case has consistently lower intensity values towards the  $-3D$  and  $-4D$  locations than the ten diameter downstream case. The greatest variation in the intensity observed by the rotors for the ten diameter downstream case, is found

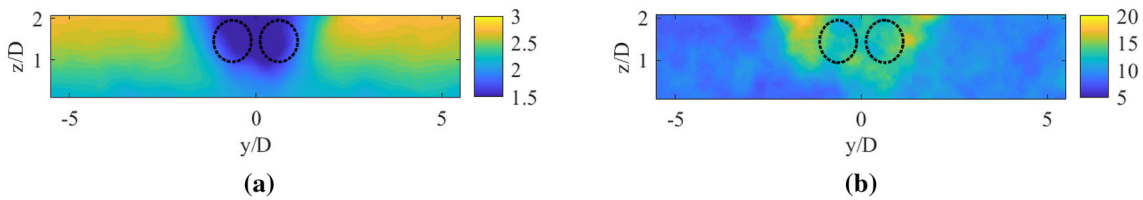


**Fig. 7** Onset flow characteristics across the plane at a distance of nine diameters behind an upstream rotor and one diameter upstream of a second device, with rotor locations shown by dashed lines. **a** Time averaged stream-wise velocity, (m/s), **b** stream-wise turbulence intensity, (%)

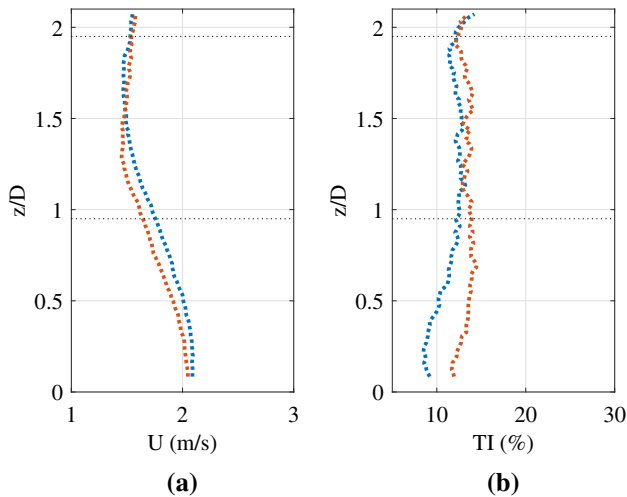


**Fig. 8** For a plane at one diameter in front of a downstream turbine, **a** vertical variation of stream-wise velocity at the centre of each rotor, **b** vertical variation of turbulence intensity at the centre of each rotor. Rotor one (blue) and rotor two (orange), height of rotor shown by dashed horizontal lines (colour figure online)

at the device position aligned with the upstream device. There is also more variation between the rotors located at  $-4D$  than expected outside of the wake. The impact of these conditions on the loading experienced on the device in these transverse locations, will also be investigated using the in-house BEM in the following Sections.

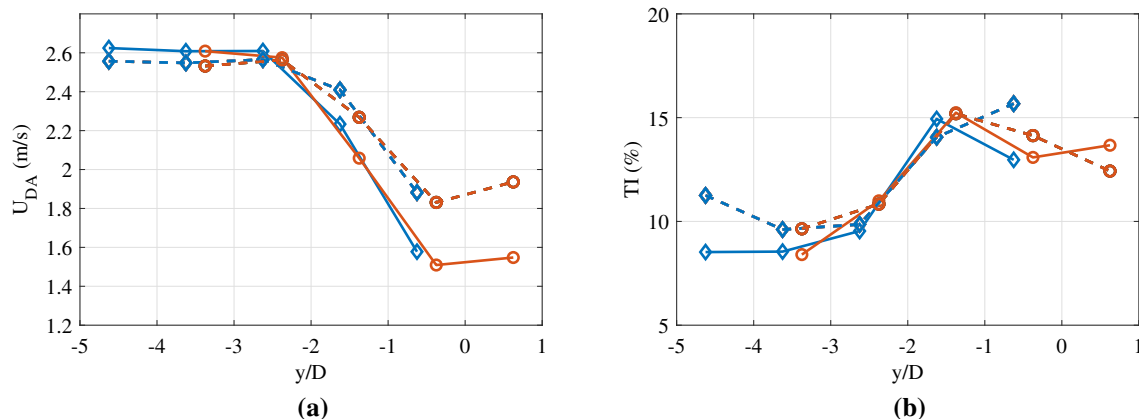


**Fig. 9** The transverse variation of disk averaged conditions where rotor one (blue) and rotor two (orange) for the nine diameters downstream plane (solid line) and ten diameters downstream (dashed line) where **a** Stream-wise velocity, **b** Turbulence intensity (colour figure online)

### 3 Loading on a single device

An initial comparison is conducted using a steady case, with a single tip-speed-ratio (TSR) chosen as previously stated in Sect. 2 of 5.5, resulting in peak  $C_P$  values representative of a full-scale device and with a difference of only 0.5%, and a 7% difference in  $C_T$  between the in-house BEM and LES-ALM respectively to the Tidal Bladed values. The onset flow generated by the LES is used as the inflow to the two rotor device, to determine the loading on the blades and the rotors. This section will compare these loads which are calculated using industry standard software - Tidal Bladed, open-source in-house BEM method and the LES-ALM from the DOFAS code.

#### 3.1 Upstream device

Initially the loading on a device is determined due to an onset flow defined purely by the ambient onset conditions, so a device is considered to be upstream. Using the methods outlined in Sect. 2 the time varying thrust loads are calculated from the combined axial force on the two blades, shown in Fig. 10. All thrust loads are normalised by the highest load value across the three methods. Observing the time varying forces, good agreement is found between the three methods, with the mean loading, defined by  $C_T$ , giving a 5% difference



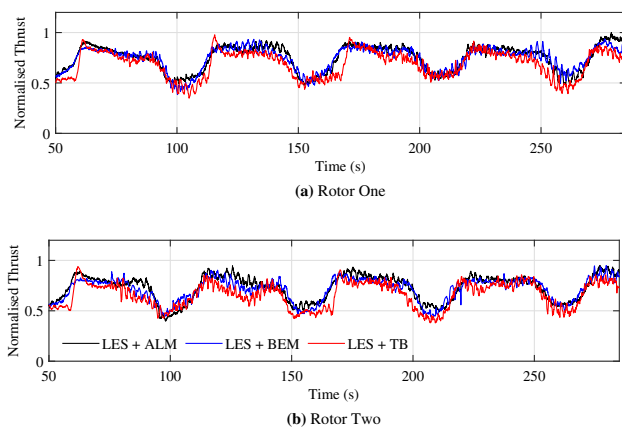


**Fig. 10** Example of time varying thrust loading for the ALM (black), in-house BEM (blue), Tidal Bladed (red), for each rotor, with mean thrust loads on average 6–20% greater for the ALM method (colour figure online)

between the ALM and the in-house BEM, and an 8% difference between the ALM and Tidal Bladed. Even though the in-house BEM method and Tidal Bladed use the same theoretical basis, there is a slight difference in the magnitude and variation of thrust loading. This could partly be attributed to a difference in time step, with the Tidal Bladed simulations having a larger value and therefore a quicker result.

The inflow for each method is considered to be consistent, with the same variation in turbulence characteristics across each rotor. However, the way in which the inflow is used to determine the loading does vary between the BEM cases and the ALM. These differences due to conditions can be seen more clearly in the load spectra, as shown in Fig. 11. Across all three methods the blade passing frequency of  $2f_0$  is observed by a peak from the thrust loading and first harmonic is also present at  $4f_0$ , where  $f_0$  is the rotor frequency. At the initial peak the magnitude of loading experienced on the rotor from all three methods is very similar, corresponding to the small difference of  $C_T$  between the methods, as the calculation of the  $C_T$  is an average from the loading. However, the time varying normalised thrust, shown in Fig. 10, does show fluctuations around the dominant periodic loading. These fluctuations are observed to provide higher magnitude load contribution to both of the BEM methods in the high frequency range ( $> 10f/f_0$ ), with Tidal Bladed having an even higher magnitude than the in-house BEM. The loading determined from the LES-ALM shows further peaks at the higher harmonics of the blade passing frequency, with the blades interacting within the flow field and therefore the potential for loading at higher frequencies, which rise above the level of noise due to the turbulence only.

In addition to determining the loading on the rotor, the blade loading is also calculated through the use of flapwise root bending moment (RBM). This is calculated using

the axial loading from both the ALM and BEM methods. Within the in-house BEM Simpson's rule is used to integrate the forces along the radius to determine the root bending moments. For all three methods an example of the time varying root bending moment is shown in Fig. 12.

The magnitude of variation is consistent between all three methods, with the mean RBM loading having a 2% difference between the blade element methods, and a 5% difference to the ALM loading, with the BEM producing a higher mean compared to the ALM, which is a reverse of the finding for the thrust force. This is due to the radial distribution of force on the blade from each method, with the differences established by a calculation of the centroid of force across the blade, with the BEM having a position 10% further along the blade, therefore higher magnitude loads are experienced further along the blade for the BEM. In comparison to the thrust loading, the RBM loading shows a more noticeable difference in the magnitude of the fluctuations between the methods used. The in-house BEM has a similar fluctuation magnitude to the ALM. The root bending moments calculated through Tidal Bladed have a greater fluctuation magnitude. This is also seen through the load spectra in Fig. 13. As with the variation of thrust, the spectra of loading for the root bending moment has been calculated for all three methods, with the rotor frequency used to normalise the frequencies. With the same inflow conditions for all three methods the interaction between the ALM and the flow field causes an increase in the magnitude of the spikes at the higher frequencies. The increase in the spectral magnitude at the high frequency range for the LES inflow to Tidal Bladed, is consistent with the load spectra shown for the thrust loading. The peak magnitude at the rotor frequency is also considerably higher for the Tidal Bladed calculated loading when compared to both the ALM and in-house BEM, with the secondary peak at the harmonic a similar magnitude between all three methods. One reason for the increase in the fluctuation magnitude for the Tidal Bladed loading results from the inclusion of the dynamic inflow in the wake model, which would account for a greater change in the loads experienced as the turbine rotates. Overall the similarities in the mean flapwise bending moments is consistent with experimental findings in McNaughton et al. (2022), where the blockage effect of a short fence has more impact on thrust than root bending moments.

For both loading spectra shown, the LES onset flows are considered using Taylor's Hypothesis of frozen turbulence for the BEM case. This results in the reduction in spikes in the spectra at the high frequency range. Overall, the BEM method has produced a load spectra which represents the load variation well compared with the LES-ALM.

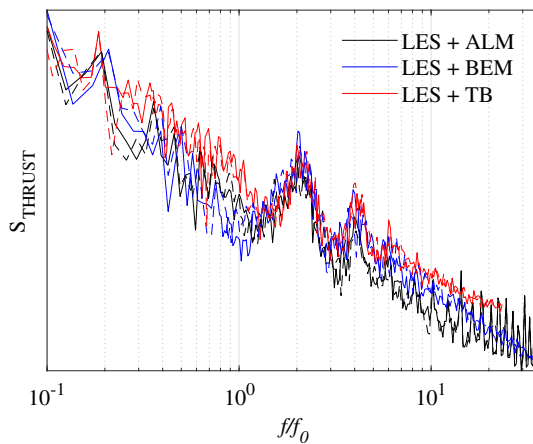


**Fig. 11** Spectra of rotor thrust loading for the ALM (black), in-house BEM (blue), Tidal Bladed (red), for each rotor, rotor one (solid lines) and rotor two (dashed lines) (colour figure online)

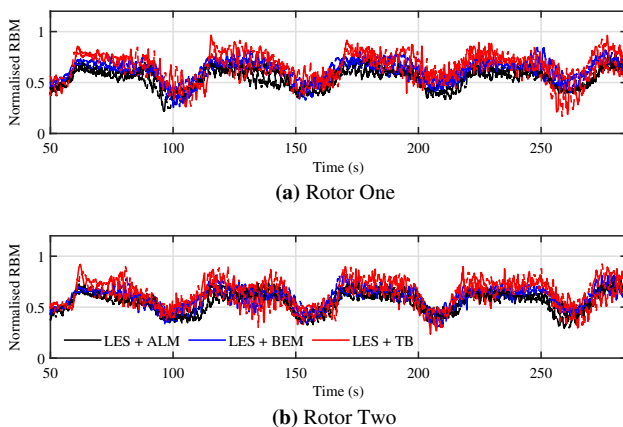


**Fig. 12** Time varying normalised root bending moment for the ALM (black), BEM (blue), Tidal Bladed (red), for each rotor. Blade one (solid lines) and blade two (dashed lines) (colour figure online)

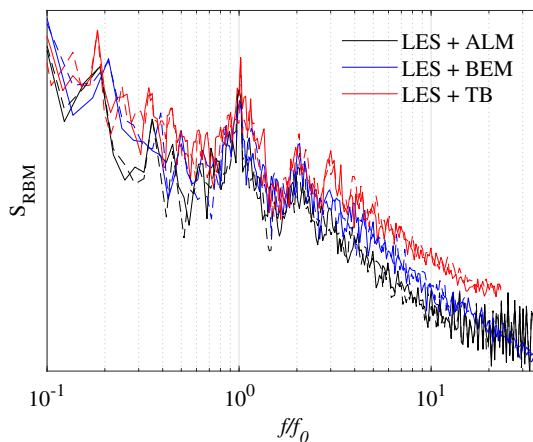


**Fig. 13** Spectra of root bending moment for the ALM (black), in-house BEM (blue), Tidal Bladed (red), for one blade on each rotor. Blade one (solid lines) and blade two (dashed lines) (colour figure online)

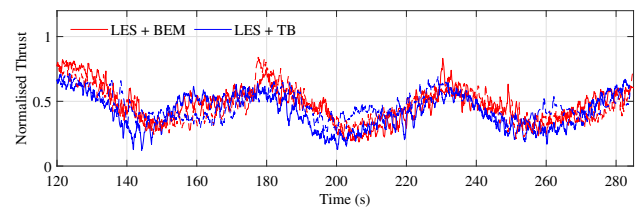


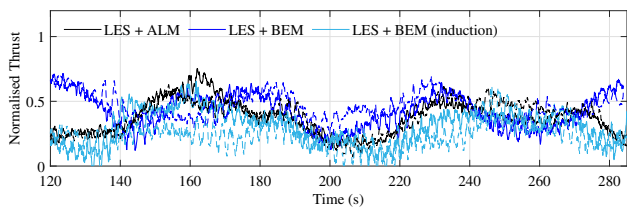
**Fig. 14** Time varying normalised thrust for the in-house BEM method (blue) and the Tidal Bladed results (red), with turbine one shown by a solid line and turbine two by a dashed line (colour figure online)

### 3.2 Downstream device

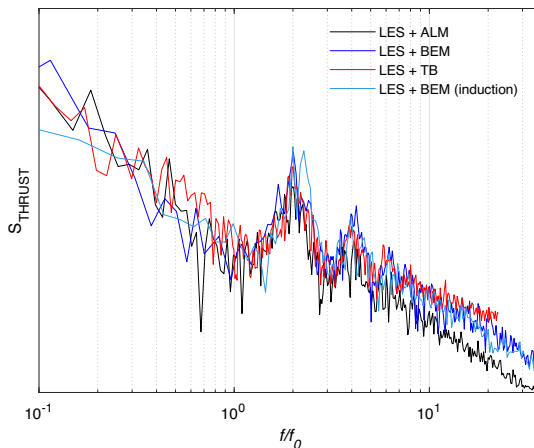
In addition to considering the loading on a single device experiencing ambient onset conditions, the loading on a second device, located in the wake region of an upstream device, is investigated. A nominal stream-wise spacing of ten turbine diameters is chosen as the distance between the two devices. The loading on this downstream device is calculated using all three methods. Initially, the downstream planes are extracted from the original LES that includes a single device upstream. This enables multiple downstream locations to be used as an inflow, as considered in Ouro et al. (2022). This onset flow plane is used as inflow to the in-house BEM and Tidal Bladed, with the thrust loading results shown in Fig. 14.

Figure 14 shows the time varying thrust normalised using the same value as the upstream turbine to facilitate comparison. These two cases use the same onset flow field which is directly inline with the upstream device and therefore experience a reduction in the mean force, due to the velocity deficit. These turbines operate at the same operating point, with a TSR of 5.5, with the velocity deficit the  $U_{DA}$  decreases as shown in Fig. 9. With the reduction in onset velocity there is a reduction in the angular velocity of the turbine to keep a constant TSR, so a larger period of rotation, which can be seen in Fig. 14 compared to Fig. 10. The thrust loading from the ALM is also shown in Fig. 15, again normalised by the maximum loading of the upstream turbine. The thrust variation from the ALM is compared to the in-house BEM calculated using a downstream plane at  $10D$ , and at  $9D$  which includes the presence of the downstream device. Based on the calculated  $U_{DA}$ , (Fig. 9), the turbine experiences a greater deficit at the  $9D$  plane. As previously seen in Figs. 5 and 7, there is a greater reduction of velocity in the wake. This means that the angular velocity of the turbine reduces further for these two cases, one reason for the differences is shown in Fig. 15.

The power spectra for the time varying loading using the two different onset flow fields are compared in Fig. 16. The overall magnitude of the load spectra for each method is consistent with the load spectra for the upstream turbines, with the loading determined using Tidal Bladed exhibiting the highest magnitude in the high frequency range. For both the in-house BEM cases the high frequency magnitudes are



**Fig. 15** Time varying normalised thrust for the in-house BEM method (blue) for ten diameters downstream as in Fig. 14, the in-house BEM method at nine diameters downstream (light blue) and the ALM (black), with turbine one shown by a solid line and turbine two by a dashed line (colour figure online)



**Fig. 16** Power spectral density of the thrust loading for each downstream case from the in-house BEM at 10 diameters (dark blue) and 9 diameters downstream (light blue). Tidal Bladed at 10 diameters downstream (red) and ALM at 10 diameters downstream (black) (colour figure online)

consistent, however, there is some variation in the magnitude over the low to mid frequencies. The peak magnitude at the blade passing frequency also has a similar magnitude between the in-house BEM cases, but a greater width of peak for the nine diameter downstream flow field, the variation of turbulence in the onset flow, combined with the shear can account for this. The thrust spectra from the ALM for the downstream device has a similar magnitude in the low frequency range, however, across the mid range at the peak frequencies (1st and 2nd harmonics) the magnitude is visibly lower, showing that the rotor blades with the ALM are not experiencing the level of shear as the BEM models. Considering the two flow fields used for the BEM codes are extracted directly from the LES, one reason for a difference in shear is a greater induction to the blade, and therefore a further reduction in velocity and potentially an adjustment of the shear profile.

The mean thrust experienced on the turbine through the different methods to calculate the loading is shown in Fig. 17. Comparing the normalised thrust for the upstream devices, there is 3–10% difference between the two BEM methods

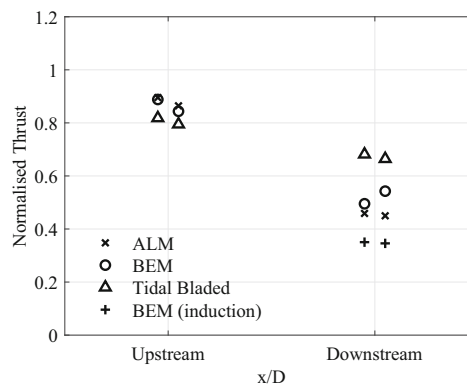


**Fig. 17** Normalised mean thrust values for each method at both upstream and downstream turbine locations. For the in-house BEM, ALM, Tidal Bladed and in-house BEM at 9D (with induction)

and less than 6% difference between the in-house BEM and the ALM. When the onset flow at ten diameters downstream is used as an inflow to the BEM methods, there is a 25–34% difference for each turbine between the mean loads. Part of the reason for the mean difference at this position could be that the larger time step leads to a greater influence of the turbulence variation within the flow field. At the downstream position, the mean loading from Tidal Bladed is 49% greater than the loads determined using the ALM model, with the in-house BEM predicting loads 10% greater. When the downstream flow field at nine diameters is used as the inflow to the in-house BEM the loads predicted are 26–29% lower than the ALM.

Damage equivalent loads (DEL) have been calculated for both the upstream and downstream cases, using the time history of thrust loading. This loading has been obtained for each method and is shown in Fig. 18. Unlike the mean thrust values, which decrease with downstream position, the damage equivalent loads increase. This is due to the greater number of load cycles, caused by an increase in the fluctuations of load due to the turbulent onset conditions in the wake. There is up to a 13% difference in the DELs between the Tidal Bladed results and the in-house BEM for the upstream devices. However, the in-house BEM for the upstream cases predicts the DEL to within 1–3% for each rotor when compared to the ALM DELs. For the downstream device, rotor one experiences the greatest variation in DEL between the in-house BEM with the ten diameter downstream flow field being 24% greater than the DEL determined from the ALM model. One reason for this difference could be due to the increase in turbulence over the original value, combined with a higher velocity value than is observed in the nine diameter downstream case, which is upstream of the ALM device. The variation between the in-house BEM and the ALM for rotor two is only 3.8%, showing that a good agreement can be found between the two methods. As the results have been

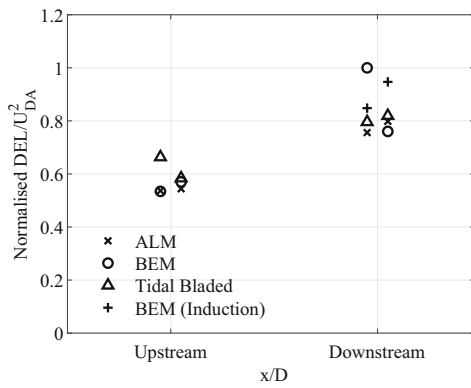


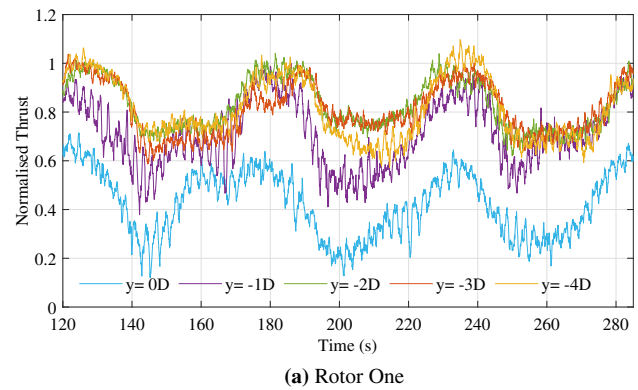
**Fig. 18** Normalised damage equivalent load variation for each method at the upstream and downstream device locations. For the in-house BEM, ALM, Tidal Bladed and in-house at  $9D$  (with induction)

normalised using the disk averaged velocity, the DEL from the nine diameters downstream in-house BEM shows closer agreement to the ten diameter downstream values, than the calculated DEL. The DEL calculated from the Tidal Bladed results for the downstream case are significantly greater than the ALM results. However the flow field has a pre-defined onset flow velocity therefore resulting in a higher disk average being applied.

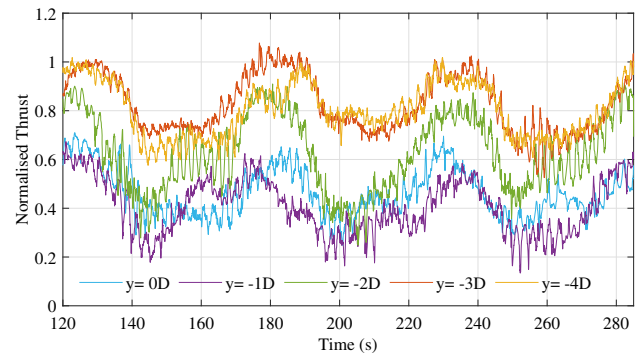
All the downstream loading results shown in Figs. 17 and 18 correspond to a device and its rotors being directly aligned with an upstream device and therefore fully immersed in the largest velocity deficit due to the wake. The next section investigates the variation of loads for a device at various transverse positions, using the in-house BEM with the two downstream flow fields from the LES to represent the inflow.

### 3.3 Offset downstream positions

This section considers the loading on a device at various transverse positions at each of the downstream locations; nine and ten diameters downstream. The variation in thrust loading on each rotor is examined to identify changes in the loading which occur as rotors are placed at different positions relative to the wake. This causes different onset flow characteristics as shown in Figs. 7 and 9 for disk averaged velocity and turbulence intensity. This section will now show the resultant thrust loads for rotors operating in those conditions with a consistent TSR. Figure 19 provides an example time history of the thrust loads for both rotors, with the rotors directly aligned to the upstream rotors at  $y = 0D$  having a lower magnitude of thrust. This is consistent for both rotors, however, the rotors at the transverse positions of  $y = -1D$  and  $y = -2D$ , have differing magnitudes, this is due to their position relative to the wake, with rotor two at  $y = -1D$  fully within the upstream wake whereas at  $y = -2D$  the rotor is in the shoulder of the wake, and still has a low disk



(a) Rotor One



(b) Rotor Two

**Fig. 19** Example time series of the normalised thrust, from the in-house BEM across the transverse rotor locations at ten diameters downstream of the initial ALM device in the LES flow field

averaged velocity. The thrust loading on the rotors at the furthest transverse positions of  $y = -3D$  and  $y = -4D$  have the same magnitude as the original upstream device loading. This is expected, as the onset flow characteristics show that the devices are operating outside of the generated wake.

The thrust load variation from the rotors using the flow field at nine diameters downstream as the inflow, is shown in Fig. 20. Due to the decrease in disk averaged velocity, as shown in Fig. 9, to keep the operating point consistent there is a reduction in the angular velocity of the rotors. This is noticeable in the variation of load when compared to Fig. 19. This difference in the flow field, results in the same trend in load magnitude across the transverse locations. Where rotor two at  $y = 0D$  and  $y = -1D$  has the same reduced magnitude as rotor one at  $y = 0D$ . For the rotors in the furthest transverse locations  $y = -3/4D$  the magnitude is comparable to the results from the ten diameter downstream cases.

The mean loads which correspond to the time variations shown in Figs. 19 and 20 are presented in Fig. 21. At  $y = 0D$  for the rotors aligned with the upstream device, the mean loads for the ALM case and the Tidal Bladed case are also shown in Fig. 21. These cases correspond to those shown in Fig. 17. As the rotors move across the transverse, the mean loads on the rotor increase, following the trend shown by the

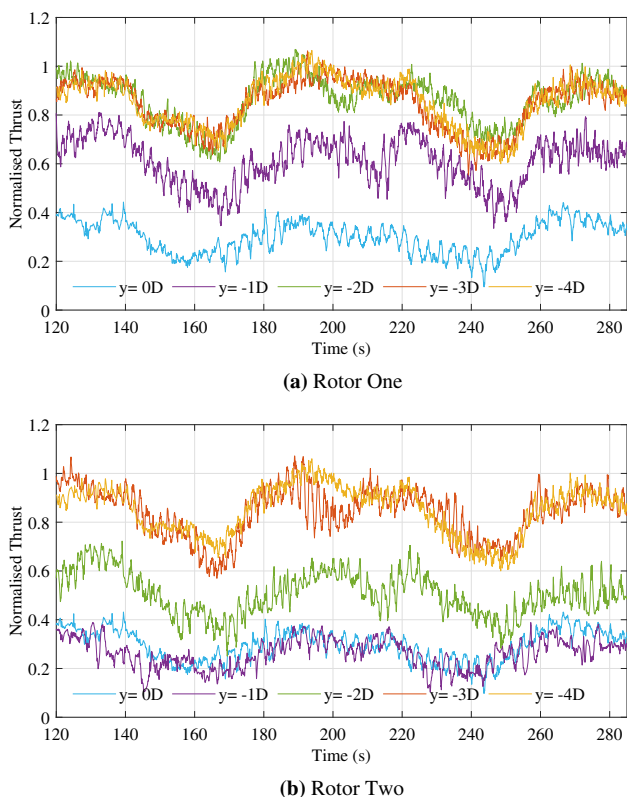


**Fig. 20** Example of the time varying normalised thrust, from the in-house BEM, across the transverse rotor locations at nine diameters downstream of the initial ALM device in the LES flow field, one diameter upstream of a second ALM device

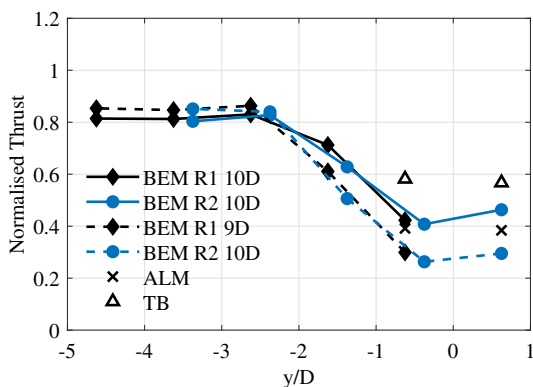


**Fig. 21** Variation of normalised mean thrust with, from the in-house BEM with transverse position, at nine diameters (dashed lines), ten diameters (solid lines). Rotor one (black) and rotor two (blue), compared to device at  $y = 0D$  for ALM results ( $\times$ ), and for Tidal Bladed ( $\Delta$ ) (colour figure online)

disk averaged velocity. At the furthest transverse positions there is a 2% difference in the loads between the either set of downstream flow fields.

The transverse variation of normalised DEL are shown in Fig. 22, calculated from both downstream flow fields. As

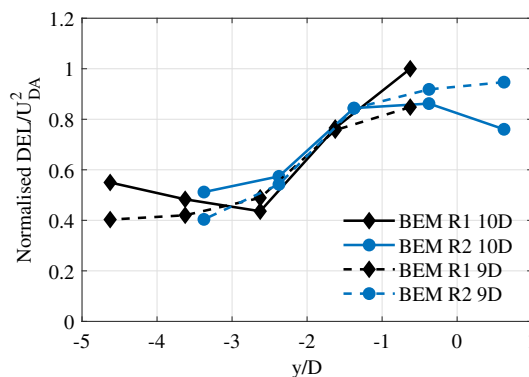


**Fig. 22** Variation of normalised damage equivalent loads across the transverse, nine diameters (dashed lines), ten diameters (solid lines). Rotor one (black) and rotor two (blue) (colour figure online)

with the mean loads there is a noticeable variation in the DELs at  $y = 0D$ , aligned with the upstream device, these loads have a mean normalised by the disk averaged velocity. By normalising the loads using the velocities the influence of the turbulence can be seen, with a 21% difference in the normalised DEL for rotor one when the device is at  $y = -4D$ . In the shoulder of the wake the normalised DELs show a consistency, a linear trend, between each method and the rotor, consistent with the trend of the disk averaged turbulence intensity, shows a dominant transverse shear profile. The next section will discuss the loading results depending on the method chosen to model the device as well as the conditions experienced in the wake.

### 3.4 Turbine operation

The loading results presented to this point are based upon fixed pitch and fixed speed turbine operation. This section explores the use of a simple pitch controller, as detailed in Sect. 2, implemented within the in-house BEM code only, to assess the impact on the statistics of the varying load. A full dynamic controller could be implemented and this would involve a variation in angular speed as well as pitch, as well as independent blade control, similar to the control methods used for wind turbines, Bianchi et al. (2006). However, here a simplified approach is taken in which the pitch of each blade can only vary by up to 1 degree to reduce peak loads, with rate of change of pitch defined by a function determined to be consistent with the output from a dynamic controller. When applied to the rotor subject to the downstream flow, this controller causes a 9% reduction in the mean and 50% reduction in the variance of the loads and hence 16% decrease in the DEL. The same controller has been applied to multiple transverse device locations and the impact on the mean and DELs are shown in Figs. 23 and 24. These Figures can be compared to Figs. 21 and 22 for the variation of loads obtained without control applied. It can be seen from Fig. 23 that when located

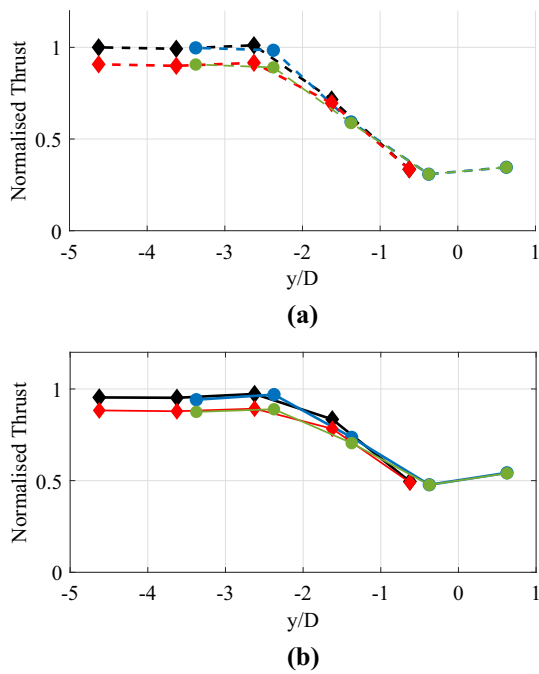


**Fig. 23** Transverse variation of normalised mean thrust on the two rotors of the device with no control applied, rotor one (black) and rotor two (blue) for (a) the nine diameter downstream flow fields given by dashed lines and (b) ten diameters downstream given by the solid lines. With control applied to rotor one (red) and rotor two (green) (colour figure online)

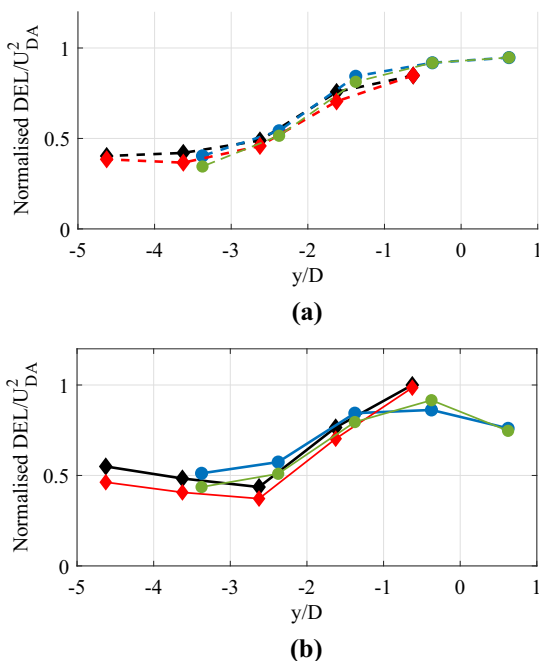


**Fig. 24** Transverse variation of normalised mean thrust on the two rotors of the device with no control applied, rotor one (black) and rotor two (blue) for (a) the nine diameter downstream flow fields given by dashed lines and (b) ten diameters downstream given by the solid lines. With control applied to rotor one (red) and rotor two (green) (colour figure online)

centrally within the flow generated by the upstream turbine, there is either no impact on the mean load or a reduction of mean load. This reduction gradually increases when rotors are positioned further away from the wake, reaching and stabilising at a 9% reduction for rotors with centres at  $y = -2D$  and  $y = -3D$ .

A similar trend to the mean load variation is observed for the variance of the unsteady rotor loads, with the rotors aligned to the wake having no change (largely as the controller does not take effect). At locations further from the wake centre-line the load variance can reduce by 50%, and this is consistent for the two downstream onset planes considered. These reductions of the mean and variance due to pitch control, result in a reduction in the DELs. The transverse variation of DELs are given in Fig. 24 for both downstream flow fields. The largest reduction in DELs is observed on the rotor positions furthest from the wake centre-line, in regions of high transverse shear, where the influence of the controller is greatest. Increasing the pitch angle variation within the controller from 1 degree to 1.5 degrees further reduces the mean and variance of the thrust loading and subsequently the DEL, by up to 18% relative to the fixed pitch case.

Further mitigation of load variation may be possible to achieve with a dynamic controller, which is implemented by most tidal turbine developers. This work is just highlighting the impact a simple controller can make on a device operating in a wake.

## 4 Discussion

Three numerical models for predicting the unsteady loading of tidal turbines have been compared using identical unsteady velocity fields as inflow to the rotors. Each unsteady onset velocity field is generated using the LES code DOFAS for a location within a turbulent open-channel flow of one diameter upstream of the device, and subsequently for locations in the wake downstream of this turbine. The turbine is represented, and blade- and rotor-loads are obtained, using an actuator line method (ALM) within DOFAS and with two implementations of a blade element method. For the latter methods, an offline coupling with the LES inflow data is done to account for realistic flow field. With two of the methods using the blade element method, there are differences in the loads calculated, with 10% variation between the two methods when considering the mean thrust loads and 5% between the mean root bending moments. When comparing these values to the mean loads on the upstream device from the ALM, there is a 3–6% difference for the thrust and 11–16% for the root bending moment.

## 4.1 Ambient turbulence

The turbulent open-channel onset flow is resolved using the DOFAS LES solver applied to a fixed depth channel with flat bed assuming smooth bed friction. At the inflow, a mean velocity profile is superimposed with fluctuating velocities defined by the Synthetic Eddy Method, Jarrin et al. (2006), to represent coherent eddies. Synthetic methods such as this are designed to enable reproduction of the turbulence characteristics developed in open-channel flows, avoiding the need for performing precursor periodic channel simulations that can be computationally expensive, Ahmed et al. (2017, 2021). Alternative formulations of synthetic inflow conditions are available, Skillen et al. (2016), Poletto et al. (2013), which differ in the extent to which a target set of turbulence characteristics can be represented, either directly or, more typically as inflow to vortex-methods (e.g. Bex et al. 2023) or to large-eddy simulations (Ahmed et al. 2017; Ouro and Stoesser 2018).

Downstream of the inflow plane, the free-stream energetic eddies propagate whilst also losing coherence into finer-scale turbulent scales and interacting with turbulence generated from the near-bed boundary layer. After travelling over relatively long distances, usually about 40 times the water depth (Nezu and Nakagawa 1994), the turbulent flow becomes fully developed, defined by the channel friction Reynolds number only. Model parameters, e.g. mesh resolution and distance from inflow plane, are selected such that the flow parameters are in an appropriate range at selected locations within the domain.

Here, the target flow characteristics are a  $1/7$ th power-law velocity profile, turbulence intensity in the range 15–10% and stream-wise turbulence length-scale in the range of  $1D$ – $2.5D$ . These ranges of turbulence intensity are representative of measurements obtained from current-profiler data for several sites, including flow-speeds greater than 1.5 m/s at Raz Blanchard (Mercier et al. 2021) and 2.0 m/s at EMEC, stream-wise length-scales are also within the ranges reported for the EMEC site, Sellar et al. (2018). Measurements of both turbulence intensity and length-scale are typically considerably higher at real deployment sites than for fully developed open-channel flows, likely due to complex mechanisms of turbulence formation at tidal stream sites including bathymetry and from eddy anisotropy developed in differing depths (Mercier et al. 2021; Ouro and Stoesser 2018). In the present simulations, the target flow characteristics develop by  $20D$  from the channel inflow, and the turbine is located at the plane  $22D$ . The development distance, and the downstream distance over which these parameters are sustained, would differ with alternative inflow formulations and with differing mesh resolution. Analysis of the channel flow only (i.e. without the turbine modelled) indicates that turbulence intensity over the swept area of the rotor is in the

range 10–12% after a channel length of around 20 times the depth, through to approximately 50 times the depth.

## 4.2 Wake recovery

Turbine load prediction is investigated due to the simulated ambient channel flow and due to the more complex combination of turbulent flow conditions that occur in a downstream wake. Experimental, numerical and theoretical analyses of wind- and tidal-turbine wakes have shown that the ambient turbulence directly influences the wake recovery rate (Ainslie 1988; Mycek et al. 2014; Parkinson et al. 2013). As such whilst our focus here is on comparing load prediction methods obtained at a specified downstream distance, the distance at which an equivalent combination of conditions would occur is sensitive to the surrounding flow conditions. The magnitude of velocity and turbulence across these onset planes is not considered to represent these locations and each plane simply provides a time-varying velocity field with spatial variation of velocity and shear such as may occur at a nominal location in a wake.

The approach taken in DOFAS adopts an SEM inflow and turbine represented with Actuator Line Method (ALM) (Ouro et al. 2019). The same numerical framework has previously been employed to obtain predictions of the wake generated by a row of three small-scale turbines, and two-row arrays of up to seven turbines, with good agreement with experimental measurements at  $4D$  and  $8D$  downstream for both the wake velocity profile and turbulence magnitude. The conditions studied in the present model have not been evaluated relative to any experimental wake data and so the downstream locations are considered to represent the features of a nominal wake only. Similar accuracy of the mean velocity profile relative to the same experiment has also been shown with RANS models (Olczak et al. 2016; Abolghasemi et al. 2016; Shives and Crawford 2017). However, whilst such approaches offer a lower computational cost than LES, RANS models cannot fully describe the time-varying velocity associated with the larger scale turbulent structures which are known to occur in tidal flows and which contribute directly to unsteady loading. These models have been widely used for wake simulation, predictions of time averaged flow but would need to be supplemented by, or used as input to, synthetic turbulence models such as Jarrin et al. (2006) to generate time-varying unsteady onset flow-fields for inflow to fatigue load prediction models.

In these simulations, the mean turbulence of the ambient flow, and therefore the flow surrounding the wake, reduces from 10% at  $0D$  to around 8% by  $10D$  downstream, with further downstream locations shown in Ouro et al. (2022). As such, whilst not quantified in this study, the rate of mixing between a wake and this ambient flow may be expected to reduce with distance downstream. To an extent, higher values

of turbulence may be generated with different inflow specification but turbulence would only be sustained over long distances (e.g.  $\gg 10D$ ) with a source of turbulence, for instance, from a rough bed. There have been some experiments to characterise tidal turbine wakes in flows with differing bed roughness (Parkinson et al. 2013) but this technique has to-date been more widely used for sustaining boundary layer atmospheric flows (e.g. Takimoto et al. 2013).

The downstream device has been shown to experience a variation in the calculated loads between the different methods, with up to a 10–18% mean thrust variation for the in-house BEM at 10 diameters downstream. When the nine diameter flow fields are used, which includes the induction from the device being modelled within the LES, there is a 26–29% variation in the mean thrust loading to the ALM loads. A better prediction is found using the computational set up with just an upstream device to generate the wake. The upstream damage equivalent loads can be predicted to within 3–5% from the in-house BEM compared to the ALM, with a greater variation at the downstream case with rotor two within 5% of the DELs calculated from the ALM, but rotor one is 32% greater. This difference is attributed to the downstream flow field variation between the rotors, with rotor one seeing a greater turbulence intensity across the rotor. Further studies could look at multiple runs to achieve an equivalent onset flow but with a different turbulence ‘seeding’.

When the downstream transverse variation of device placement is considered, the rotors are shown to experience varying mean and fatigue loads. This is demonstrated to show the use of the in-house BEM in determining loading within an array of turbines. The loading clearly varies with the change in onset flow conditions, when moving between in-wake to out-of-wake placement, with mean thrust loading decreasing with the reduction in disk averaged velocity and damage equivalent loads increasing potentially due to the increase in turbulence intensity which leads to greater load fluctuations contributing to the number of load cycles. This leads to a variation of up to 67% across the transverse locations for the mean thrust and up to 54% difference for the damage equivalent loads. When modelling to determine device positions in an array the variation in fatigue loads should be taken into account as well as any methods which can be used to mitigate. However, it is worth noting that the velocity deficit for the wake from a floating tidal device has not previously been modelled and validated based on site conditions, this study is using an LES code which has previously been validated against another set of experiments. Further work will look into the impact of turbulence on wakes and the influence of site features such as bathymetry on the development and dissipation of the wakes from these devices.

## 5 Conclusions

This work presents a combination of multiple computational methods to predict the loading on a tidal turbine undergoing full scale turbulent flow conditions. Results show that the loads predicted using an Actuator Line model within a high fidelity large-eddy simulation can be calculated to within 5% accuracy using an unsteady blade element momentum theory code, when the onset LES flow fields are used in both cases. The similarities between the loading from the ALM and from the in-house BEM for the upstream device gives confidence that the efficient BEM can be used as an alternative to a full LES simulation with embedded model for each turbine to provide loads. The time saving aspect of the comparison is realised when looking at the loading of a device subject to the more complex flow regime within a wake. The ALM within the LES resolves the interaction between the device and the flow field, forming a wake region in which helical tip vortices can initially be observed and which recovers through mixing with the ambient flow. Whilst the typical features associated with a wake are observed, the locations within the wake at which loads are analysed are chosen to show the complicated mix of flow phenomena that occur only. These are not representative of conditions at specific distances within real turbine wakes since the ambient turbulence conditions generated by SEM inflow and the flat bed over the extent of the wake differ from ambient flows at tidal sites. Differences in wake recovery would be expected with more representative turbulence in the ambient flow along the extent of the wake. This analysis shows that the loading of turbines within the complex unsteady flows that occur in wakes can be achieved to high accuracy without explicitly modelling all devices with the LES-ALM approach, thus reducing compute time required to assess loading for alternative array layouts. This approach also facilitates investigation of alternative operating strategies, without explicitly modelling the device within the LES-ALM approach. Implementation of a simple pitch control algorithm in the in-house BEM code, accounting for variation with onset flow speed, is shown to reduce the fatigue loads experienced on the rotors. There is an optimum variation of pitch angle which reduces the DEL through the mean and variance of the loads. This can be further investigated to determine whether consistent loading can be experienced across an array of turbines if different levels of pitch control are used.

**Author Contributions** HM—modelling, writing—original draft, review and editing. LA—modelling, review and editing. CM—review and editing. PO—modelling, writing—original draft, review and editing. TS—funding acquisition, writing—original draft, review and editing.

**Funding** This work is supported by the Tidal Stream Industry Energiser project (TIGER), co-financed by the European Regional Development Fund through the INTERREG France (Channel) England Programme. The authors would like to acknowledge the support provided by the



Research IT from the Computational Shared Facility at The University of Manchester. This work used the ARCHER2 UK National Supercomputing Service (<https://www.archer2.ac.uk>).

**Data availability statement** Onset flow fields used in this work, for two of the cases, are available at <https://doi.org/10.48420/24518191>.

## Declarations

**Ethical Approval** Not applicable.

**Conflict of interest** Authors declare no Conflict of interest.

**Open Access** This article is licensed under a Creative Commons Attribution 4.0 International License, which permits use, sharing, adaptation, distribution and reproduction in any medium or format, as long as you give appropriate credit to the original author(s) and the source, provide a link to the Creative Commons licence, and indicate if changes were made. The images or other third party material in this article are included in the article's Creative Commons licence, unless indicated otherwise in a credit line to the material. If material is not included in the article's Creative Commons licence and your intended use is not permitted by statutory regulation or exceeds the permitted use, you will need to obtain permission directly from the copyright holder. To view a copy of this licence, visit <http://creativecommons.org/licenses/by/4.0/>.

## References

- Abolghasemi M, Piggott MD, Spinneken J, Viré A, Cotter CJ, Crammond S (2016) Simulating tidal turbines with multi-scale mesh optimisation techniques. *J Fluids Struct* 66:69–90. <https://doi.org/10.1016/j.jfluidstructs.2016.07.007>
- Afgan I, McNaughton J, Rolfo S, Apsley D, Stallard T, Stansby P (2013) Turbulent flow and loading on a tidal stream turbine by LES and RANS. *Int J Heat Fluid Flow* 43:96–108. <https://doi.org/10.1016/j.ijheatfluidflow.2013.03.010>
- Ahmed U, Apsley D, Afgan I, Stallard T, Stansby P (2017) Fluctuating loads on a tidal turbine due to velocity shear and turbulence: comparison of CFD with field data. *Renew Energy* 2:235–246. <https://doi.org/10.1016/j.renene.2017.05.048>. arXiv:arXiv:1011.1669v3
- Ahmed U, Apsley D, Stallard T, Stansby P, Afgan I (2021) Turbulent length scales and budgets of Reynolds stress-transport for open-channel flows; friction Reynolds numbers  $Re_\tau = 150, 400$  and 1020. *J Hydraul Res* 59(1):36–50. <https://doi.org/10.1080/00221686.2020.1729265>
- Ainslie JF (1988) Calculating the flowfield in the wake of wind turbines. *J Wind Eng Ind Aerodyn* 27(1–3):213–224
- Apsley DD, Stansby PK (2020) Unsteady thrust on an oscillating wind turbine: Comparison of blade-element momentum theory with actuator-line CFD. *J Fluids Struct* 98:103141. <https://doi.org/10.1016/j.jfluidstructs.2020.103141>
- Bex CC, Dufour M, Belkacem YB, Pinon G, Germain G (2023) Tidal and wind turbine simulation with the simulation code DOROTHY. In *Trends in Renewable Energies Offshore*, Volume V, pp. 113–122
- Bianchi FD, De Battista H, Mantz RJ (2006) *Wind turbine control systems*. Springer, London. <https://doi.org/10.1007/1-84628-493-7>
- Díaz-Dorado E, Carrillo C, Cidras J, Román D, Grande J (2021) Performance evaluation and modelling of the Atir marine current turbine. *IET Renew Power Gen* 15:821–838. <https://doi.org/10.1049/rpg.2.12071>
- DNV-GL (2015) Standard: Tidal Turbines (DNVGL-ST-0164). Technical Report October
- Downing SD, Socie DF (1982) Simple rainflow counting algorithms. *Int J Fatigue* 4(1):31–40. [https://doi.org/10.1016/0142-1123\(82\)90018-4](https://doi.org/10.1016/0142-1123(82)90018-4)
- Garcia-Novo P, Kyojuka Y (2017) Field measurement and numerical study of tidal current turbulence intensity in the Kobe Strait of the Goto Islands, Nagasaki Prefecture. *J Mar Sci Technol* 22:335–350. <https://doi.org/10.1007/s00773-016-0414-x>
- Garcia-Novo P, Kyojuka Y (2019) Analysis of turbulence and extreme current velocity values in a tidal channel. *J Mar Sci Technol* 24:659–672. <https://doi.org/10.1007/s00773-018-0601-z>
- Harrold M, Ouro P (2019) Rotor loading characteristics of a full-scale tidal turbine. *Energies* 12(6):1035. <https://doi.org/10.3390/en12061035>
- Jarrin N, Benhamadouche S, Laurence D, Prosser R (2006) A synthetic-eddy-method for generating inflow conditions for large-eddy simulations. *Int J Heat Fluid Flow* 27(4):585–593. <https://doi.org/10.1016/j.ijheatfluidflow.2006.02.006>
- Martínez Tossas L, Churchfield M, Meneveau C (2018) Optimal smoothing length scale for actuator line models of wind turbine blades based on Gaussian body force distribution. *Wind Energy* 2:1083–1096. <https://doi.org/10.1002/we.2081>
- Masters I, Malki R, Williams AJ, Croft TN (2013) The influence of flow acceleration on tidal stream turbine wake dynamics: A numerical study using a coupled BEM-CFD model. *Appl Math Model* 37(16–17):7905–7918. <https://doi.org/10.1016/j.apm.2013.06.004>
- McNaughton J, Cao B, Nambiar A, Davey T, Vogel CR, Willden RHJ (2022) Constructive interference effects for tidal turbine arrays. *J Fluid Mech* 943:1–31. <https://doi.org/10.1017/jfm.2022.454>
- Mercier P, Grondeau M, Guillou S, Thiébot J, Poizot E (2020) Numerical study of the turbulent eddies generated by the seabed roughness. Case study at a tidal power site. *Appl Ocean Res*. <https://doi.org/10.1016/j.apor.2020.102082>
- Mercier P, Guillou S (2021) The impact of the seabed morphology on turbulence generation in a strong tidal stream. *Phys Fluids* 33:5. <https://doi.org/10.1063/5.0047791>
- Milne IA, Sharma RN, Flay RGJ, Bickerton S (2013) Characteristics of the turbulence in the flow at a tidal stream power site. *Philos Trans R Soc A Math Phys Eng Sci* 371:1985. <https://doi.org/10.1098/rsta.2012.0196>
- Mullings H, Draycott S, Thiebot J, Guillou S, Mercier P, Hardwick J, Thies P, Stallard T (2023) Evaluation of model predictions of the unsteady tidal stream resource and turbine fatigue loads relative to multi-point flow measurements at Raz Blanchard. *Energies* 16:1–33. <https://doi.org/10.3390/en16207057>
- Mullings H, Stallard T (2019a) Unsteady loading in a tidal array due to simulated turbulent onset flow. In *Advances in Renewable Energies Offshore - Proceedings of the 3rd International Conference on Renewable Energies Offshore, RENEW 2018, Number 2006*, pp. 227–235
- Mullings H, Stallard T (2021) Assessment of dependency of unsteady onset flow and resultant tidal turbine fatigue loads on measurement position at a tidal site. *Energies* 14(17):1–13. <https://doi.org/10.3390/en14175470>
- Mullings H, Stallard T (2022) Analysis of tidal turbine blade loading due to blade scale flow. *J Fluids Struct* 114:103698. <https://doi.org/10.1016/j.jfluidstructs.2022.103698>
- Mullings HR, Stallard T (2019b) Assessment of tidal turbine load cycles using synthesised load spectra, including blade-scale fluctuations. In *13th European Wave and Tidal Energy Conference*, pp. 1–9
- Mycek P, Gaurier B, Germain G, Pinon G, Rivoalen E (2014) Experimental study of the turbulence intensity effects on marine current turbines behaviour. Part I: One single turbine. *Renew Energy* 66:729–746. <https://doi.org/10.1016/j.renene.2013.12.036>

- Nezu I, Nakagawa H (1994) Turbulence in open-channel flows. *J Fluid Mech* 269:373–374. <https://doi.org/10.1017/S0022112094211618>
- Olczak A, Stallard T, Feng T, Stansby PK (2016) Comparison of a RANS blade element model for tidal turbine arrays with laboratory scale measurements of wake velocity and rotor thrust. *J Fluids Struct* 64:87–106. <https://doi.org/10.1016/j.jfluidstructs.2016.04.001>
- Orbital Marine Power (2022) The O2 device. <http://orbitalmarine.com/o2/>. [Online; accessed 01-05-2022]
- Ouro P, Macleod A, Mullings H, Stansby P, Stallard T (2023) High-fidelity modelling of a six-turbine tidal array in the Shetlands. *Proceedings of 15th European Wave and Tidal Energy Conference, 3-7 September 2023, Bilbao, Spain*. <https://doi.org/10.36688/ewtec-2023-442>
- Ouro P, Mullings H, Christou A, Draycott S, Stallard T (2024) Wake characteristics behind a tidal turbine with surface waves in turbulent flow analyzed with large-eddy simulation. *Phys Rev Fluids* 9(3):34608. <https://doi.org/10.1103/PhysRevFluids.9.034608>
- Ouro P, Mullings H, Stallard T (2022) Establishing confidence in predictions of fatigue loading for floating tidal turbines based on large-eddy simulations and unsteady blade element momentum. *Trends Renew Energy Offshore* 2:915–924. <https://doi.org/10.1201/9781003360773-101>
- Ouro P, Nishino T (2021) Performance and wake characteristics of tidal turbines in an infinitely large array. *J Fluid Mech* 925:A30. <https://doi.org/10.1017/jfm.2021.692>
- Ouro P, Ramirez L, Harrold M (2019) Analysis of array spacing on tidal stream turbine farm performance using Large-Eddy Simulation. *J Fluids Struct* 91:102732. <https://doi.org/10.13140/RG.2.2.35271.75682>
- Ouro P, Stoesser T (2018) Impact of environmental turbulence on the performance and loadings of a tidal stream turbine. *Flow Turbul Combust*. <https://doi.org/10.1007/s10494-018-9975-6>
- Parkinson S, Thomson M (2013) PerAWAT WG3WP4 D19: Tidal-farmer model validation and uncertainties. Technical report, PerAWAT WG3WP4 D19
- Parkinson SG, Collier WJ (2016) Model validation of hydrodynamic loads and performance of a full-scale tidal turbine using Tidal Bladed. *Int J Marine Energy* 16:279–297. <https://doi.org/10.1016/j.ijome.2016.08.001>
- Pitt DM, Peters DA (1980) Theoretical prediction of dynamic-inflow derivatives. In *Sixth European Rotorcraft and Powered Lift Aircraft Forum*, Number, p 47
- Poletto R, Craft T, Revell A (2013) A new divergence free synthetic eddy method for the reproduction of inlet flow conditions for les. *Flow Turbul Combust* 91(3):519–539. <https://doi.org/10.1007/s10494-013-9488-2>
- Sellar BG, Wakelam G, Sutherland DR, Ingram DM, Venugopal V (2018) Characterisation of tidal flows at European Marine Energy Centre in the absence of ocean waves. *Energies*. <https://doi.org/10.3390/en11010176>
- Shen WZ, Mikkelsen R, Sørensen JN, Bak C (2005) Tip loss corrections for wind turbine computations. *Wind Energy* 8:457–475. <https://doi.org/10.1002/we.153>
- Shives M, Crawford C (2017) Tuned actuator disk approach for predicting tidal turbine performance with wake interaction. *Int J Marine Energy* 17:1–20. <https://doi.org/10.1016/j.ijome.2016.11.001>
- Skillen A, Revell A, Craft T (2016) Accuracy and efficiency improvements in synthetic eddy methods. *Int J Heat Fluid Flow* 62:386–394. <https://doi.org/10.1016/j.ijheatfluidflow.2016.09.008>
- Stallard T, Collings R, Feng T, Whelan J (2013) Interactions between tidal turbine wakes: experimental study of a group of three-bladed rotors. *Philos Trans R Soc A Math Phys Eng Sci* 371(1985):20120159–20120159. <https://doi.org/10.1098/rsta.2012.0159>
- Stansby P, Stallard T (2016) Fast optimisation of tidal stream turbine positions for power generation in small arrays with low blockage based on superposition of self-similar far-wake velocity deficit profiles. *Renew Energy* 92:366–375. <https://doi.org/10.1016/j.renene.2016.02.019>
- Stansby PK, Ouro P (2022) Modelling marine turbine arrays in tidal flows. *J Hydraul Res* 60:187–204. <https://doi.org/10.1080/00221686.2021.2022032>
- Takimoto H, Inagaki A, Kanda M, Sato A, Michioka T (2013) Length-scale similarity of turbulent organized structures over surfaces with different roughness types. *Bound-Layer Meteorol* 147(2):217–236. <https://doi.org/10.1007/s10546-012-9790-x>
- Togneri M, Lewis M, Neill S, Masters I (2017) Comparison of ADCP observations and 3D model simulations of turbulence at a tidal energy site. *Renew Energy* 114:273–282. <https://doi.org/10.1016/j.renene.2017.03.061>
- Togneri M, Pinon G, Carlier C, Choma Bex C, Masters I (2020) Comparison of synthetic turbulence approaches for blade element momentum theory prediction of tidal turbine performance and loads. *Renew Energy* 145:408–418. <https://doi.org/10.1016/j.renene.2019.05.110>
- Veers P (1988) Three-dimensional wind simulation. Technical report. Sandia National Laboratories, California
- Weller SD, Thies PR, Gordelier T, Johanning L (2015) Reducing reliability uncertainties for marine renewable energy. *J Marine Sci Eng* 3:1349–1361. <https://doi.org/10.3390/jmse3041349>

**Publisher's Note** Springer Nature remains neutral with regard to jurisdictional claims in published maps and institutional affiliations.